Microstructure control of CrN_x films during high power impulse magnetron sputtering

Grzegorz Greczynski, Jens Jensen, J Bohlmark and Lars Hultman

Original Publication:

Grzegorz Greczynski, Jens Jensen, J Bohlmark and Lars Hultman, Microstructure control of CrN_x films during high power impulse magnetron sputtering, 2010, SURFACE and COATINGS TECHNOLOGY, (205), 1, 118-130.
http://dx.doi.org/10.1016/j.surfcoat.2010.06.016

Microstructure control of CrN_x films during High Power Impulse Magnetron Sputtering

G. Greczynski[1*], J. Jensen[1], J. Böhlmark[2], and L. Hultman[1]

[1] *Thin Film Physics Div., Department of Physics (IFM), Linköping University, SE-581 83, Sweden*
[2] *Sandvik Tooling RTC, Lerkrogsvägen 19, SE-126 80 Stockholm, Sweden (previously at Chemfilt Ionsputtering AB)*

ABSTRACT

The microstructure and composition of CrN_x ($0 \le x \le 1$) films grown by reactive High Power Pulsed Magnetron Sputtering (HIPIMS or HPPMS) have been studied as a function of the process parameters: N_2-to-Ar discharge gas ratio, ($f_{N2/Ar}$), negative substrate bias (V_s), pulsing frequency, and energy per pulse. The film stoichiometry is found to be determined by the composition of the material flux incident upon the substrate during the active phase of the discharge with no nitrogen uptake between the high-power pulses. Scanning electron microscopy investigations reveal that for $0 < f_{N2/Ar} < 0.15$ and 150 V bias, a columnar film growth is suppressed in favor of nano-size grain structure. The phenomenon is ascribed to the high flux of doubly charged Cr ions and appears to be a unique feature of HIPIMS. The microstructure of column-less films for $100\,\mathrm{V} \le V_S \le 150\,\mathrm{V}$ is dominated by the Cr(N) and hexagonal β-Cr_2N phases and shows a high sensitivity to the V_s. As the amplitude of V_s decreases to 40 V and self-biased condition, the film morphology evolves to a dense columnar structure. This is accompanied by an increase in the average surface roughness from 0.25 nm to 2.4 nm. CrN_x samples grown at $f_{N2/Ar} \ge 0.3$ are columnar and show high compressive stress levels ranging from -7.1 GPa at $f_{N2/Ar} = 0.3$ to -9.6 GPa at $f_{N2/Ar} = 1$. The power-normalized deposition rate decreases with increasing pulse energy, independent of $f_{N2/Ar}$. This effect is found to be closely related to the increased ion content in the plasma as determined by optical emission spectroscopy. The HIPIMS deposition rate normalized to DC rate decreases linearly with increasing relative ion content in the plasma, independently of $f_{N2/Ar}$ and pulsing frequency, in agreement with the so-called target-pathways model. Increasing frequency leads to a finer grain structure and a partial suppression of the columnar growth, what is attributed to the corresponding increase of the time-averaged mean energy of film-forming ions arriving at the substrate.

keywords: high power pulsed magnetron sputtering; HPPMS; high power impulse magnetron sputtering; HIPIMS; CrN; magnetron sputtering

*- corresponding author: grzgr@ifm.liu.se

address:

Department of Physics (IFM)
Thin Film Physics Division
Linköping University
SE-581 83, Sweden;
phone: +46 13 28 1213;

1. INTRODUCTION

High power impulse magnetron sputtering (HIPIMS or HPPMS) is a sputtering technique that relies on the creation of high-density plasma in front of the sputtering source [1]. The increase in plasma density is achieved by increasing the peak power applied to the target in short (typically less than 100 μs) pulses, with a low (a few percent) duty factor. Since the thermal load of the target is limited by the average power rather than the peak power, the latter quantity can be very high during the active phase of a discharge. The applied voltage can reach a couple of kV, resulting in a peak discharge current density of the order of a few A/cm^2 and a peak power density of several kW/cm^2. This results in electron densities exceeding 10^{19} m^{-3} in the vicinity of the magnetron [2-4]. The high density of electrons increases the probability for electron impact ionization of the sputtered atoms, and results in a highly ionized flux of target material [1, 3, 5]. The high degree of ionization opens new opportunities for film design, since the ions may be controlled by the use of electric and magnetic fields [6] through ion-surface interactions. Specially, the energy of film-forming ions arriving at a surface may be steered by the use of a substrate bias, which strongly affects the properties of the growing film [7]. A high degree of target ion content created in the vicinity of the target surface is a reason for the commonly observed drop in the deposition rate [8-10] which has been associated with the HIPIMS technique. This is in contrast to the conventional ionized PVD where the secondary plasma is created away from the target to ionize the flux of sputtered atoms on its way to the substrate [11]. The former effect is believed to be caused by the fact that a certain fraction of the ionized flux of target material is back-attracted by the cathode field, which results in a severe rate drop especially for materials characterized by low self-sputtering yields [12, 13].

Up to date HIPIMS has been used in the reactive mode to deposit a number of industrially-attractive coatings [14-23]. Despite the still growing number of publications dealing with characterizations of thin films prepared using this technique a basic parameter study revealing the nature of the reactive HIPIMS processing is missing.

The focus of this work is the effect on the film growth from process parameters that are unique to HIPIMS, namely pulsing frequency (*f*), energy delivered to the target in each pulse (E_p) and pulsed substrate bias (V_S). Cr-N was chosen as a model system due to the limited reactivity of Cr towards nitrogen (resulting in a high partial pressure required for a turnover from metallic to nitrided target state), which allows for a better control of film composition while investigating the relationship between the flow of reactive gas and the pulsing frequency [24]. In contrast, N-rich CrN_x films have been deposited by a number of sputtering techniques and are relatively well characterized [25-31].

2. EXPERIMENTAL

All film depositions were performed in an industrial CC800/9 coating system manufactured by CemeCon AG in Germany [32]. The base pressure of the vacuum chamber is 2×10^{-3} Pa. A single rectangular Cr target of dimensions 88×500 mm² was sputtered in Ar/N_2 atmosphere. HIPIMS power supplies integrated into the coating unit were employed, except for the part of the studies on dependence of substrate bias in Sec. *3.3,* where the cathode was operated by an external Sinex 3 power supply manufactured by Chemfilt Ionsputtering AB, Sweden. Control experiments indicated no significant dependence of the resulting film microstructure on the type of power supply used. Silicon (001) wafers with a native oxide layer were used as substrates. Prior to depositions, the substrates were ultrasonically cleaned in acetone

and isopropanol. For each film, the deposition process consisted of the following steps: (1) radiation heating (2 kW heating power for 30 min.), (2) radiation heating (0.5 kW heating power for 30 min.) resulting in the substrate temperature, $T_s \approx 200$ °C and the background pressure of the order of 1-2 mPa, (3) deposition of a ~30 nm thick Cr film in order to improve adhesion and reduce stress at the substrate interface (heating power kept at 0.5 kW), and (4) deposition of CrN_x films (typically: 40 min. at 300 Hz and scaled correspondingly for other frequencies to keep the total number of pulses constant). All films were deposited at the constant total pressure of 0.4 Pa. Resulting film thickness was in the range from 0.8 to 2.1 μm, depending on the amount of nitrogen in the sputtering gas mixture. The peak power levels achieved in these experiments were of the order of 240 kW, resulting in the peak power density of 0.55 kW/cm^2 (calculated for the whole target area) while the average power density did not exceed 5.2 W/cm^2. A Tektronix DPO4054 500 MHz bandwidth digital oscilloscope was used to monitor and record the current and voltage transients during all depositions.

Elemental composition of the films was measured by Time-of-Flight Elastic Recoil Detection Analysis (ToF-ERDA) at the Tandem Laboratory in Uppsala, Sweden. The primary ion beam was 40 MeV $^{127}I^{9+}$ ions, the recoil scattering angle was 45°, and the incident angle was 67.5° relative to the surface normal. The obtained TOF-ERDA data were evaluated using the CONTES code [33]. Cross-sectional electron microscopy investigations were carried out on fractured films using LEO 1550 FEG scanning electron microscope. The crystalline structure was determined by XRD with a Bruker AXS D8 Advance diffractometer operated in θ–2θ mode using Cu Kα radiation. For each sample, a set of θ–2θ scans was recorded at the tilt angle, ψ, scanned between 0° and 85° (in steps of 5°) allowing for (i) accurate identification of crystal phases present, (ii) determination of film texture, and (iii) residual stress estimation by the $\sin^2 \psi$

method using Young modulus values derived from nanoindentation tests (E varying between 281.5 GPa and 323.6 GPa) and the Poisson ratio, $\nu = 0.2$, in order to be consistent with other authors [26]. Since tilting of the sample affects the paths of incident and diffracted X-ray beams, all θ–2θ scans were corrected with the absorption factors according to the procedure described in [34]. AFM was performed using a Veeco Dimension 3100 instrument with a Nanoscope IIIa controller. The optical emission spectroscopy (OES) signal was measured in the line-of-sight geometry with the probe placed outside the port window of the chamber (cf. [32]) and directed towards the race track. Here, a spectrometer (Mechelle Sensicam 900) connected to a collimator via an optical fiber was used to record the emission from the plasma. The spectral range of the spectrometer was 300-1100 nm. The shutter speed of the spectrometer was set to 100 ms allowing for data averaging over multiple HIPIMS pulses. Measured line intensities were corrected for transition probabilities and level degeneracy using the database by Kurucz *et al.* [35] and following a procedure described elsewhere [5, 36].

The pulse energy, E_p, is defined here as the integral of the product of target current, $I(t)$, and target voltage, $V(t)$, over the pulse period, $T = 1/f$, $E_p = \int_0^T dt V(t) I(t)$. It is emphasized that any variation of E_p corresponds to change in the value of the peak target current, as the pulse width is kept constant at 200 μs.

3. RESULTS AND DISCUSSION

This part of the paper is organized as follows. In Sec. *3.1* film growth rates and film compositions for different pulsing frequencies are analyzed as a function of $f_{N2/Ar}$ (at the constant total pressure of 0.4 Pa) with the help of cross-sectional SEM and ToF-ERDA. Important aspects

of kinetics during film formation are discussed including the issue of inter-relation between nitrogen partial pressure, pulsing frequency, and resulting film composition. For this analysis, E_p was chosen such that a significant ionization of the target material could be achieved (roughly one-to-one ratio in the bulk of the plasma, as determined by OES). The frequency was set in the middle of the power supply specification (300 Hz) in order to allow for potential adjustments later on. The negative sample bias, V_s, was set relatively high (150 V) in order to manifest ion bombardment effects, in case any differences should appear while varying $f_{N2/Ar}$. The rest of the paper is divided into sections discussing changes in the film microstructure as a function of: gas composition (Sec. *3.2*), substrate bias (Sec. *3.3*), pulse energy (Sec. *3.4*), and pulsing frequency (Sec. *3.5*). The samples of relevance are listed in Table 1 along with essential process parameters.

3.1 Film growth and composition

The changes in deposition rate with increasing nitrogen fraction in the sputtering gas mixture are shown in Fig. 1A, whereas trends in the resulting film composition are depicted in Fig. 1B. Similar to conventional reactive sputtering, an increased flow of reactive gas leads to a drop in the deposition rate of the HIPIMS process due to the target poisoning. However, in contrast to DC operation, where the condition of the target is determined by the flow of the reactive gas, an additional "knob" exists in the present case; namely that of the pulsing frequency. It is a unique feature of reactive HIPIMS that the typical pause between the pulses (usually 1-10 ms) matches quite well monolayer formation times for typically used partial pressures of the reactive gas (of the order of 0.1 – 1.0 Pa). This means that the degree of target poisoning may be steered by varying the pulsing frequency allowing for (some) control over the growth rate (per pulse) and the nitrogen content in the film. This is illustrated in Fig. 1A. A comparison between

Table 1 List of all CrN_x samples mentioned in the main text along with relevant information. "C" and "CF" in the "growth mode" column stand for columnar and column-free growth modes, respectively.

	$f_{N2/Ar}$	f [Hz]	E_p [J]	V_S [V]	N [at.%]	phase	texture	growth mode	stress [GPa]
A	0	300	13.3	150	0	α-Cr	[210]	C	-1.46
A2	0	300	13.3	selfbias	0	α-Cr	[200]	C	N/A
B	0.02	300	13.3	150	4.9	Cr(N)	[210]	CF	-3.71
B2	0.02	100	13.3	150	23	β-Cr_2N	[111]	CF	N/A
B3	0.05	300	13.3	150	16.1	Cr(N)+**β-Cr_2N**	[111]	CF	-2.62
C	0.1	300	13.3	150	28.8	Cr(N)+**β-Cr_2N**	[111]	CF	N/A
C2	0.1	100	13.3	150	34.3	CrN	CrN[220]	CF/C	N/A
C3	0.1	100	13.3	selfbias	45.8	CrN	-	C	-2.34
C4	0.1	300	13.3	selfbias	34	β-Cr_2N	β-Cr_2N[111]	C	N/A
C5	0.1	500	13.3	selfbias	31.3	β-Cr_2N	β-Cr_2N[111]	CF/C	N/A
C6	0.1	500	13.3	150	27.3	β-Cr_2N	β-Cr_2N[111]	CF	N/A
D	0.15	300	13.3	150	33.4	**β-Cr_2N**+CrN	CrN[220]	CF/C	N/A
E	0.2	300	13.3	150	38.8	**CrN**+β-Cr_2N	slight[111]	C	-9.48
E2	0.2	500	13.3	150	34.6	β-Cr_2N	[111]	CF	N/A
F	0.3	300	13.3	150	43.6	CrN	[111]	C	-7.07
F3	0.3	100	13.3	150	45	CrN	[111]	C	N/A
F2	0.3	500	13.3	150	45.1	CrN	[111]	C	-3.41
G	0.5	300	13.3	150	44.3	CrN	[111]	C	-8.40
G2	0.5	300	13.3	selfbias	49.4	CrN	slight[220]	C	-4.82
G3	0.5	500	13.3	150	44.2	CrN	[111]	C	N/A
H	0.75	300	13.3	150	46.9	CrN	[111]	C	-7.85
I	1	300	13.3	150	47	CrN	[111]	C	-9.64
I2	1	300	13.3	selfbias	50.4	CrN	[220]	C	-4.63
J	2	300	13.3	150	47	CrN	[111]	C	N/A

the growth rates obtained at different frequency indicates that, indeed, the deposition rate per pulse scales with increasing pulsing frequency, independent of $f_{N2/Ar}$. The difference is particularly significant between 100 Hz and 300 Hz, while very subtle between 300 Hz and 500 Hz. Similar trends are also observed for self-biased films as discussed below.

The film composition determined from ToF-ERDA is shown in Fig. 1B. As expected, for a given pulsing frequency and sample bias, a decreasing deposition rate correlates to an increasing amount of atomic nitrogen in the film. For example, films grown at f = 300 Hz and V_s = 150 V (red curve) exhibit an increasing nitrogen content with increasing nitrogen flow

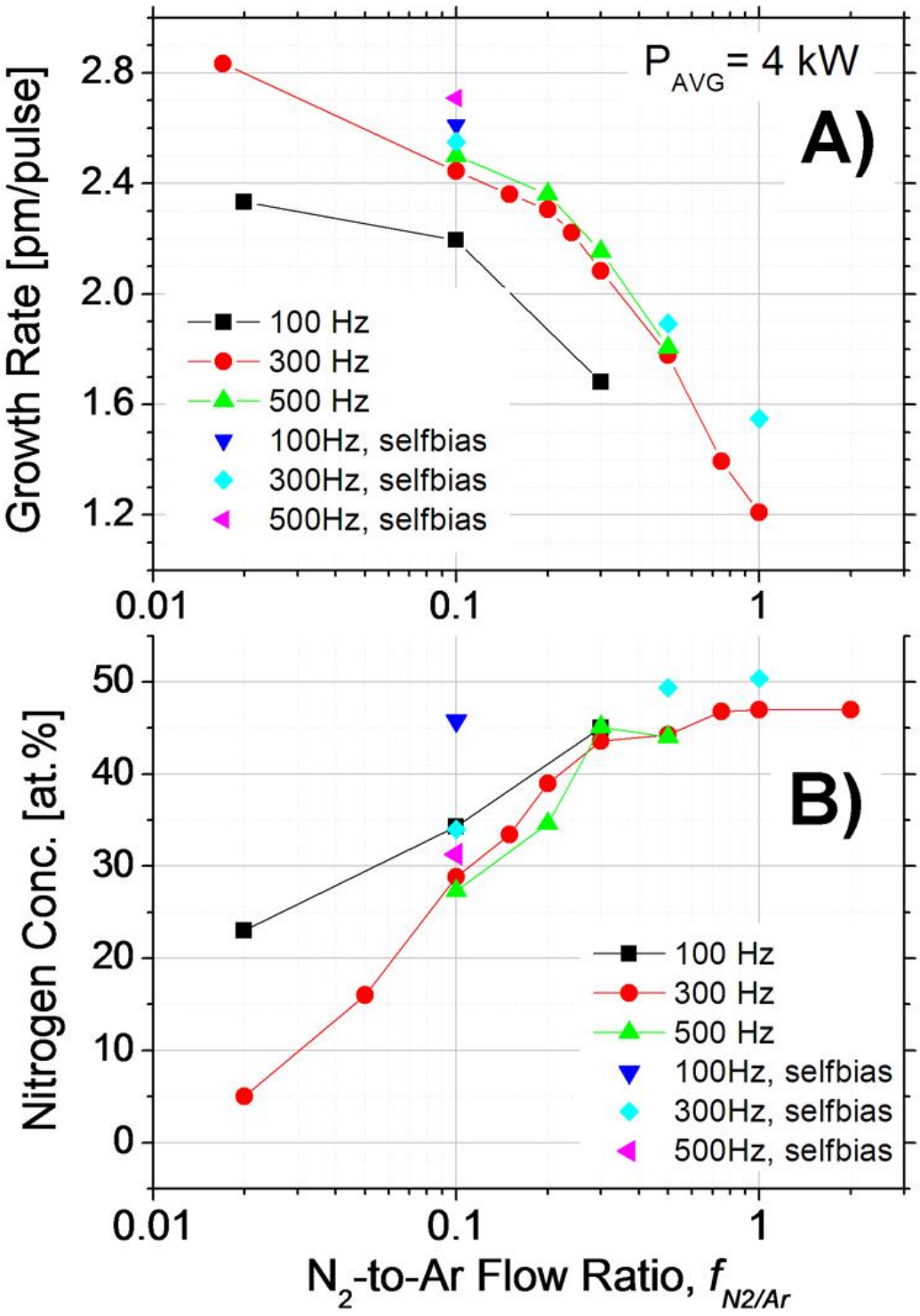

Figure 1 Film growth rate (A) and nitrogen content (B) as a function of $f_{N2/Ar}$. If not explicitly written negative bias voltage of 150 V was applied. Growth rate per pulse is calculated as the film thickness (from SEM fracture cross-section) divided by the total number of pulses during deposition.

up to $f_{N2/Ar}$ = 0.3 that saturates above that at ~46 at.%. This slight understoichiometry is ascribed to the high substrate bias used, as evident from the fact that films grown on floating substrates reach 50 at.% nitrogen at higher $f_{N2/Ar}$. The effects related to the biasing are treated in more detail in Sec. *3.3*. The composition of coatings grown at different pulsing frequency correlates well to previously described trends in deposition rates. A significantly lower growth rate (per pulse) in the 100 Hz films is associated with higher concentrations of atomic N at a given flow rate, $f_{N2/Ar}$. At the same time the observed difference in nitrogen content between films grown at 500 Hz and at 300 Hz is within experimental error. While discussing the amount of nitrogen in the sample one should consider that the surface reaction on the substrate may also take place between the pulses, during each millisecond-long break. However, simple estimates show that if the ambient N_2 should react with the freshly deposited film with similar rate as on the target, stoichiometric films would have been obtained already at $f_{N2/Ar} \leq 0.002$. This is because, as indicated in Fig. 1A, the amount of Cr delivered in each pulse is still small (oscillates around 1/100 of a ML) relative to the amount of N_2 molecules impinged on the substrate during the pulse off time. These observations are in agreement with literature. It was thus shown by Ensinger et al. [37] that freshly deposited Cr does not react spontaneously with N_2 to form CrN_x at T<500 K. The composition of the present coatings thus agrees with the predictions based on the assumption that most of the film-forming atoms/ions are sputter-ejected from the target. This is corroborated by our mass spectroscopy studies performed in parallel [38]. A high flux of energetic N^+ ions synchronized in time with Cr^+ (and Cr^{2+}) emission was observed. Both the time dependence and energy distribution of these ions suggest that they originate from the target. Moreover, during the most energetic part of the pulse the N_2^+ ions experience a severe drop in intensity, what further

reduces the chances for potential contribution to growing film from the alternative source of reactive nitrogen species (N ions are first to react with deposited Cr before any N_2 molecules). In addition, the CrN^+ fragments were also detected, but at much lower rates. It is therefore very likely that most of the nitrogen found in the films was first captured by the hot target surface (predominantly in the period between the pulses) and then became sputter-ejected and (partially) ionized on the way to the substrate. This energetic flux of reactive N^+ ions and atomic nitrogen is well timed with the highly ionized metal flux Cr^+/Cr^{2+} further enhancing chances for a compound formation on the substrate. Thus, it can be stated that the amount of nitrogen in the film depends on frequency due to the fact that the condition of the target shows such dependency. The nature of inter-relation between the degree of target poisoning and the pulsing frequency is, however, complex (as evident from the presented data), since not only the reaction time, but also reactivity towards nitrogen are affected by the frequency. Finally, it is emphasized that the present case should be distinguished from the situation where the film composition is determined by the reaction on the substrate during the pulse off time, which may very well take place for other more reactive combinations of reactive gas and target material (e.g., Ti and N_2). Nevertheless in the case of CrN_x (and presumably other materials that do not react spontaneously with sputtering gases), HIPIMS does not have any advantage over conventional DC sputtering in terms of a lower consumption of the reactive gas necessary to form a stoichiometric nitride.

In connection with the gas-substrate reactivity issue discussed above it can also be noted that ToF-ERDA results indicated a very low oxygen content in the films, usually not exceeding 0.1 at.%. This is surprising taking into account the fact that the depositions were performed at the background pressure of the order of 1-2 mPa, thus within the regime where ML formation times are matching the time gap between the high-power pulses. In addition no Ar impurities were found in any of the films, meaning that they are below the detection limits of 0.1

at.%. This is in contrast to the reference CrN_x samples prepared by a conventional DC sputtering, where the Ar content varied between 0.1 at.% and 0.3 at.%. This phenomenon can be explained with the help of ion mass spectroscopy [38], which revealed a severe drop in the intensity of the Ar^+ ion flux during the high-power pulse. The latter was caused by a high flux of sputter-ejected species entering the plasma, leading to both gas rarefaction and quenching of the electron energy distribution function. As a result, the total Ar^+ ion count rate experienced an intensity drop in the middle of the pulse. This, combined with the fact that the substrate bias was only applied during the 200 μs long voltage pulse to the cathode, significantly lowered the chances for Ar incorporation into the growing film.

3.2 Dependence on gas composition

Fig. 2 shows fracture cross-section SEM micrographs of coatings grown at E_p = 13.3 J, f = 300 Hz, and V_s = 150 V as a function of $f_{N2/Ar}$. The purely metallic film (A) shows a columnar structure with a typical signature of the competitive growth, which results in conical grains and a rough surface. The addition of small amounts of nitrogen to the gas mixture leads to radical changes in the coating microstructure. Already at $f_{N2/Ar}$ = 0.02 (sample B in Fig. 2), corresponding to 5 at.% N in the film, the columnar growth is suppressed and the film is composed of a nano-sized grains. Similar structures are obtained within the range $0 < f_{N2/Ar} < 0.15$ (B-D), thus for nitrogen contents lower than 33 at.%. The column-free growth mode results in an extremely flat surface topography that hardly gives any contrast in SEM (cf. AFM results below). The film prepared at $f_{N2/Ar}$ = 0.15 (D) shows some indications of a columnar growth, that becomes even more visible in case of the next sample in this series (E, $f_{N2/Ar}$ = 0.2). Increasing $f_{N2/Ar}$ beyond

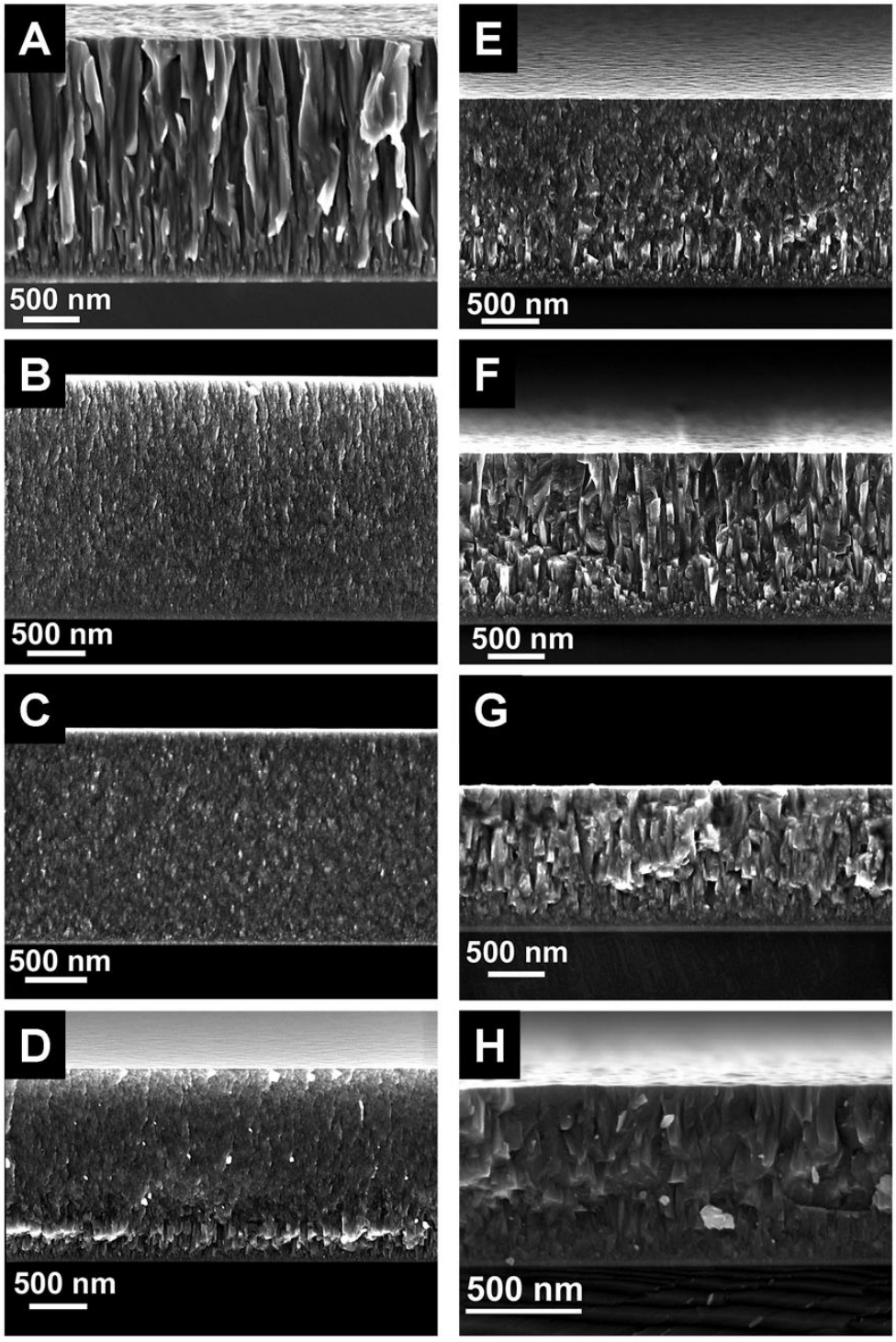

Figure 2 Fracture cross-section SEM micrographs from films grown with increasing $f_{N2/Ar}$: A) 0, B) 0.02, C) 0.1, D) 0.15, E) 0.2, F) 0.3, G) 0.5, and H) 0.75. Deposition parameters were: E_p = 13.3 J, f = 300 Hz, V_s = 150 V and T_s = 200 ^{o}C. Note the different scale used in the case of $f_{N2/Ar}$ = 0.75 (H).

0.2 brings back the signature of a columnar growth that fully develops at $f_{N2/Ar}$ = 0.3 (F, 44 at.% nitrogen) and persists in all high-nitrogen content samples (G-H).

Feature-free SEM cross-sections of CrN_x films deposited using UBM technique were reported by Hurkmans *et al.* [28], for T_s = 250 °C and V_s = 100 V, similar to our study. The suppression of columnar growth was, however, restricted to samples dominated by the β-Cr_2N phase, with the nitrogen content varying between 20 at.% and 33 at.%. Samples with lower nitrogen content (7.5 at.%) and higher nitrogen content (46.5 at.%) were characterized by a dense columnar structure. Such results were also obtained by Rebholz *et al.* [30] (T_s = 200 °C and V_s = 50 V) who observed dense, feature-less SEM cross-sections at 29 at.% nitrogen. XRD data presented in [30] revealed formation of a solid solution Cr(N) in the case of films with lower nitrogen content (between 7 at.% and 16 at.%) where columnar growth was found. Thus, while the transition from the column-free to columnar growth when going beyond 33 at.% nitrogen content agrees well with our results (cf. Fig. 2C-F), the suppression of columnar growth observed for Cr(N) solid solutions containing as little as 5 at.% of nitrogen is unique to HIPIMS.

The crystal phases present in the series of CrN_x coatings were characterized by means of θ-2θ XRD scans performed at the tilt angle ψ, varying between 0° and 85°, in steps of 5°. The reason for using this approach is that we encountered large peak shifts when varying the tilt angle, which makes standard polar figure measurements not feasible. This type of studies also supplies information about the crystalline structure of the material that could easily be missed in a simple θ-2θ scan. This is illustrated in Fig. 3, where a set of θ-2θ XRD scans for the nano-crystalline film grown at $f_{N2/Ar}$= 0.1 is shown (cf, sample C in Fig. 2). While the scan performed at the tilt angle ψ = 0° is almost structure-less (only a small bump around 2θ = 43°), measurements performed at higher angles reveal the presence of the hcp β-Cr_2N phase. By

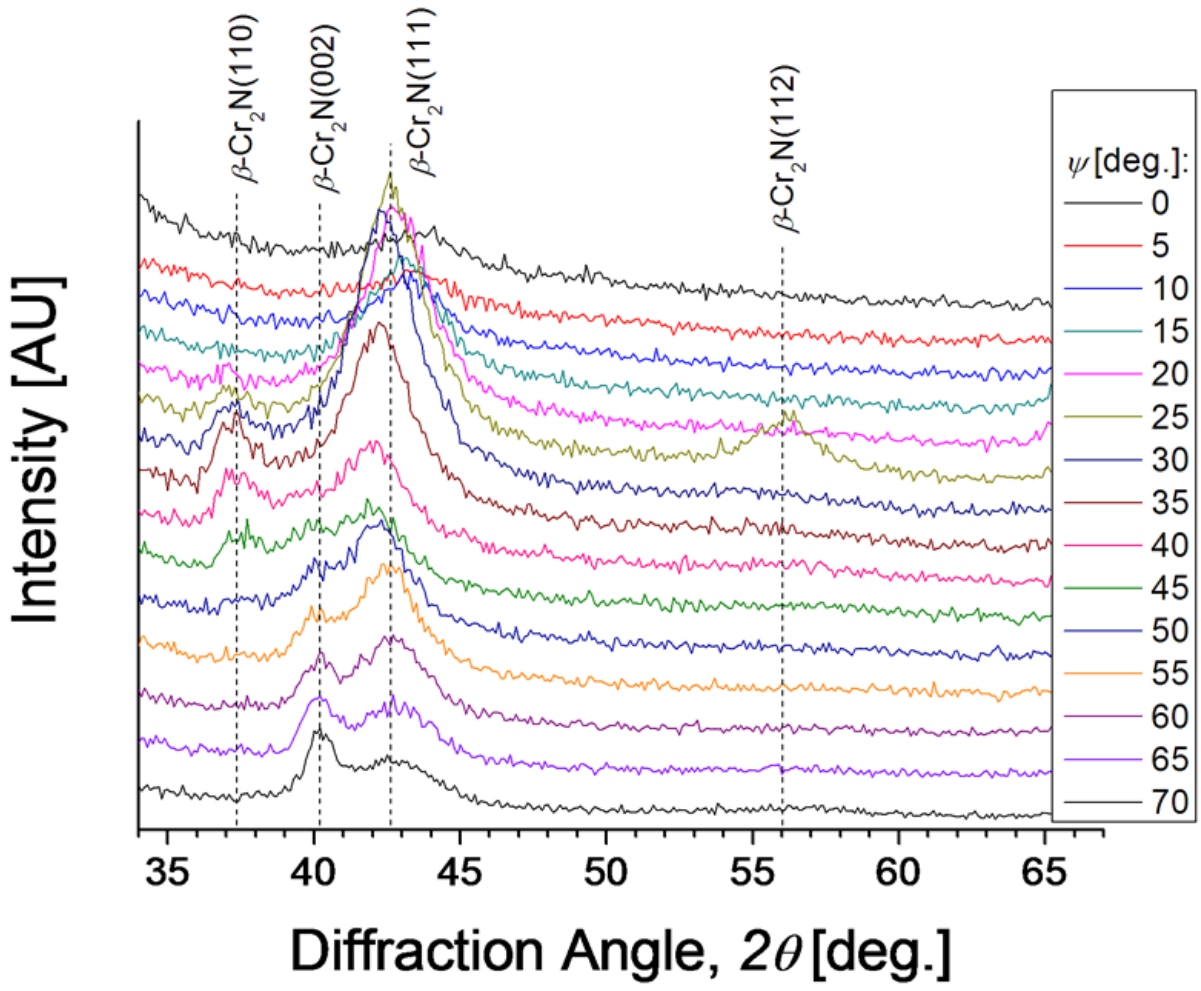

Figure 3 θ–2θ XRD scans performed as a function of the tilt angle, ψ for sample denoted as "C" in Fig. 2 and Table 1 ($f_{N2/Ar}$ = 0.1, E_p = 13.3 J, f = 300 Hz, V_s = 150 V).

applying the same method to all other CrN_x samples in this series, the evolution of crystalline content (crystal phases and their orientation) with increasing $f_{N2/Ar}$ could be mapped out (see Table 1). Starting with the metallic sample (A in Fig. 2), a θ-2θ scan at ψ = 0° shows only one prominent peak at the diffraction angle 2θ = 44.27° corresponding to the (110) reflection of the bcc Cr lattice, shifted towards lower angle with respect to the tabulated values, by 0.12°. However, closer analysis of the area variations of the (110) peak as a function of ψ, reveals three

maxima (appearing at around 18°, 51° and 71°) that match the inter-planar angles between (110) and (210) lattice planes. Therefore, it is suggested that despite the apparent (110) peak at $\psi = 0°$, the film posses the ⟨210⟩ texture. The residual stress level calculated by the d-sin$^2\psi$ method [34] using the (110) reflection indicates a rather low compressive stress of -1.5 GPa. The sample with the lowest nitrogen content (sample B, $f_{N2/Ar}$= 0.02) exhibits also only a (110) diffraction peak at $\psi = 0°$. However, in this case the peak is significantly broader (FWHM of 1.7°) and shifted towards a lower diffraction angle (43.80° at $\psi = 0°$). Severe peak broadening is the consequence of a nano-crystalline growth, as indicated above by the SEM micrographs in Fig. 2. The average crystallite size estimated from the line broadening using Sherrers formula is 5 nm. Peak shift, on the other hand, is attributed to the expansion of the original bcc Cr lattice upon nitrogen incorporation, and results in the residual stresses amounting to -3.7 GPa. It is thus evident that, despite a drastically reduced crystallite size and a column-free growth mode, the original bcc Cr lattice is preserved and nitrogen is predominantly occupying the interstitial sites forming a Cr(N) solid solution.

β-Cr_2N is first detected in the sample containing 16 at.% nitrogen (sample B3, $f_{N2/Ar}$= 0.05, cf. Table 1) where it co-exists with Cr(N), what is in good agreement with the phase equilibrium diagram for film formation at temperatures lower than 500 °C [39].

For $f_{N2/Ar}$= 0.1 (sample C in Fig. 2 containing 29 at.% nitrogen), the set of XRD spectra in Fig. 3 shows a predominant β-Cr_2N phase. The average size of crystallites contributing to the diffracted signal is calculated to be 3.2 nm. The sample is still understoichiometric as for the single-phase film. It is therefore assumed that other phases, like a solid solution Cr(N) may still be present. The broad feature present at around 44° diffraction angle in the scan taken at $\psi =$

0° (black curve in Fig. 3) could, in fact, be due to the (110) reflection coming from the very fine grains of Cr(N).

With increasing nitrogen content up to 33 at.% ($f_{N2/Ar}$= 0.15, sample D) the film is dominated by the β-Cr_2N phase with a contribution from ⟨220⟩-textured CrN crystallites. The texture of the hexagonal phase can not be determined due to the overlap with CrN signal. It is worth to emphasize that this sample marks the onset of a transition from the column-free growth mode to the columnar growth typically observed for samples with higher nitrogen content. The occurrence of the CrN phase above 33 at.% nitrogen is in agreement with Ref. [39].

Further increase of the nitrogen content produces films dominated by the CrN phase (with residues of β-Cr_2N) and with more pronounced columnar growth (cf. $f_{N2/Ar}$= 0.2, sample E containing 39 at.% nitrogen). Along with this, the average crystallite size increases and in sample E it is estimated to 5.4 nm. The more pronounced XRD signal allows for reliable estimates of the residual stress level – analysis of the CrN(111) peak shift with varying tilt angle yields high compressive stress value of -9.5 GPa. Starting from the sample denoted as F in Fig. 2 (grown at $f_{N2/Ar}$= 0.3 and containing 44 at.% N) and moving towards higher N_2 flows, all films are characterized by a single CrN phase, columnar growth (cf. Fig. 2 F, G, H), and strong ⟨111⟩ texture. The compressive stress levels in this regime are between -7.1 GPa at $f_{N2/Ar}$ = 0.3 and up to -9.6 GPa at $f_{N2/Ar}$ = 1 and the average crystallite size exceeds 10 nm. These values of residual stress, although very high, are in good agreement with previously reported numbers where a combination of energetic deposition and a high substrate bias was used. Odén et al. [26] reported the residual stress of -8.8 GPa for arc-deposited CrN films at 100 V bias, while Sáfrán et al. [21] measured -9.5 GPa for CrAlYN/CrN nano multilayers prepared by HIPIMS with V_s = 150 V.

3.3 Dependence on substrate bias

We begin this section with a discussion on the CrN_x films grown at $f_{N2/Ar}$= 0.1, i.e., at the process point where a 150 V bias results in the mixed-phase films composed of fine grains of Cr(N) and β-Cr_2N. The effect of varying substrate bias on film microstructure is illustrated in Fig. 4 where fracture cross-section SEM micrographs are shown for V_s ranging between 40 V and 150 V (pulsed bias synchronized with the cathode pulse). Films prepared at floating potential are also included in this comparison. Similar to current and voltage traces, the floating potential also exhibits a variation during the high-power pulse. In some cases, the self-bias was observed to temporary reach 100 V and more during the initial phase of the discharge (due to electrons streaming out from the cathode before any ion current flows), and dropping after that as the ions are collected. The amplitude of the floating potential was observed to decrease with increasing pulsing frequency, which can be explained by plasma decay times on the ms scale [40] as seen of ion mass spectroscopy measurements. The higher frequency pulsing should thus result in a higher plasma density right before the pulse. Hence, there will be a higher density of thermalized ions that can partially neutralize charged surfaces leading to lower floating potentials. We conclude that there is no direct parallel to the common term "floating potential" as it is used in conventional DC sputtering.

The micrographs shown in Fig. 4 indicate that the film microstructure is highly sensitive to the applied bias voltage. As the amplitude of V_s decreases the film morphology evolves from the column-free ($100\,\mathrm{V} \le V_S \le 150\,\mathrm{V}$) through some intermixed growth mode stage ($60\,\mathrm{V} \le V_S \le 80\,\mathrm{V}$) into a dense columnar structure observed at V_s = 40 V and for the self-biased films. The corresponding changes in the surface topography are illustrated with 1×1 μm AFM micrographs in Fig. 5. It can be seen that films grown at V_s = 150 V are characterized by an

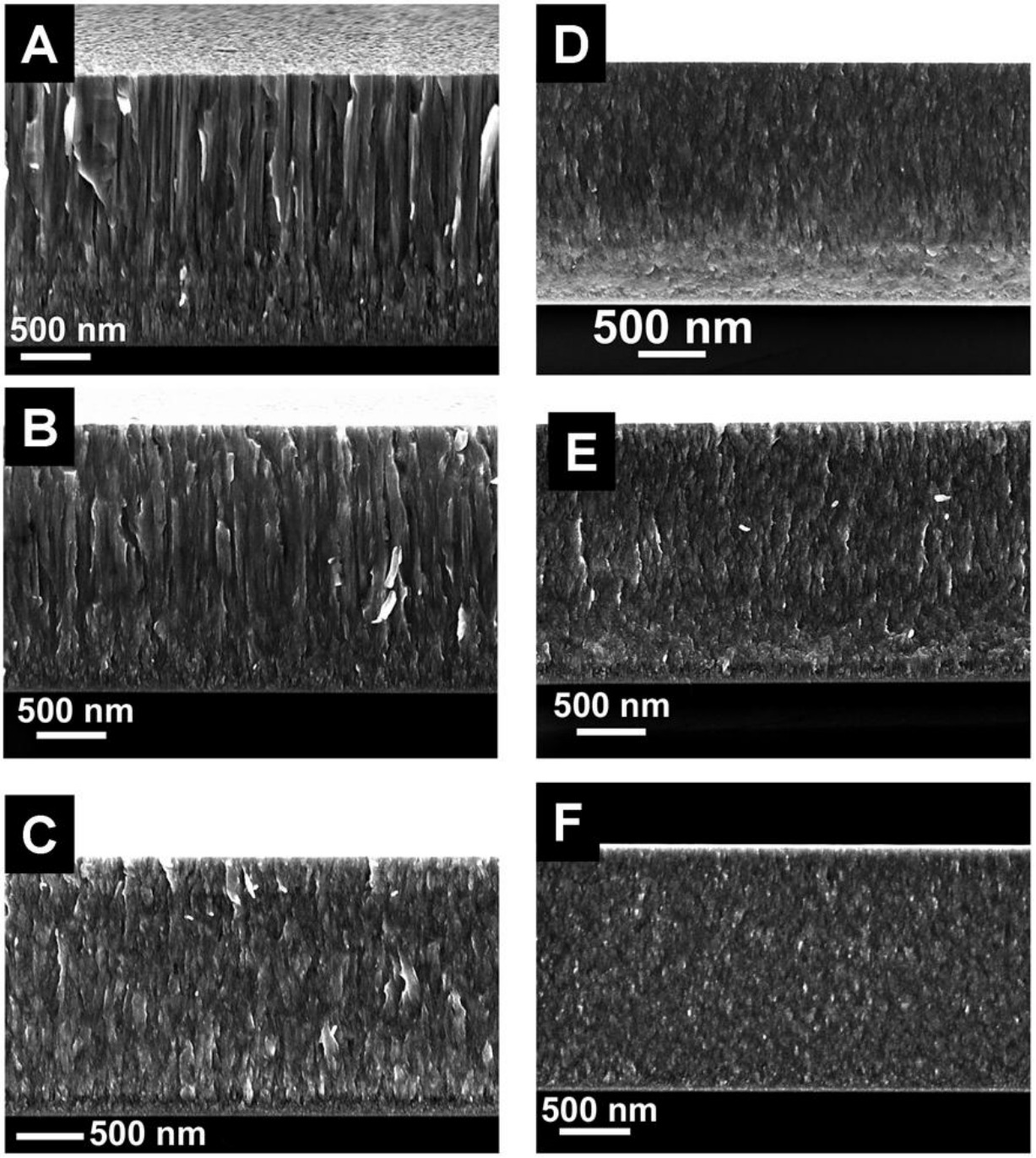

Figure 4 Effect of substrate bias at $f_{N2/Ar}$ = 0.1 illustrated with fracture cross-section SEM micrographs for different negative substrate bias voltage, V_S: A) self-bias, B) 40 V, C) 60 V, D) 80V, E) 100 V, and F) 150 V.

extremely flat surface with the surface roughness essentially on the atomic level - the average surface roughness, R_a, amounts to only 0.25 nm for the total film thickness of 1.76 μm. The

evolution in the growth mode from the column-free at high bias to a columnar at lower bias is also reflected in the surface topography: The surface roughness increases dramatically due to the shadowing effects from the growth of column facets, as can be seen in the AFM scans of Fig. 5. The average surface roughness and root mean square roughness increase approximately 10-fold while going from V_s = 150 V to the self-bias condition. The ψ-dependent θ-2θ XRD scans performed on this set of samples (not shown apart from the case of V_s = 150 V data displayed in Fig. 3) indicate that the self-bias sample (denoted as "C4" in Table 1) is dominated by the β-Cr_2N phase with extreme ⟨111⟩ texture and relatively large grains giving rise to strong narrow spectral peaks. Upon increasing substrate bias the amplitude of the XRD signal gradually decreases indicating decreasing grain size, in agreement with the SEM observations. Eventually, at V_s = 150 V, the sample is composed of small grains of Cr(N) and β-Cr_2N that yield low signal levels as evident from Fig. 3. The nitrogen content in the self-biased sample increases to 34 at.% (with respect to 29 at.% at V_s = 150 V) indicating that the re-sputtering effect are by far less severe, despite high temporal amplitude of the floating potential. Even though the nitrogen content in this sample is slightly higher than in the case of the film prepared at $f_{N2/Ar}$ = 0.15 and V_s = 150 V ("D"), the CrN phase is not detected.

The effect of substrate bias on films prepared under lower ($f_{N2/Ar}$ = 0, samples "A" and "A2") and higher ($f_{N2/Ar}$ = 0.5, samples "G" and "G2") N_2 flows is presented in Figures 6 and 7, respectively. As evident from the SEM micrographs both Cr metal films as well as the CrN films show columnar growth, independently of the applied bias (150 V vs self-bias). Thus, in this respect they behave differently from films dominated by the β-Cr_2N phase, as discussed above. The substrate bias has, however, a clear effect on the film texture (cf. Fig. 7). While going from the floating potential to V_s = 150 V the preferred orientation changes from ⟨200⟩ to ⟨210⟩ (cf.

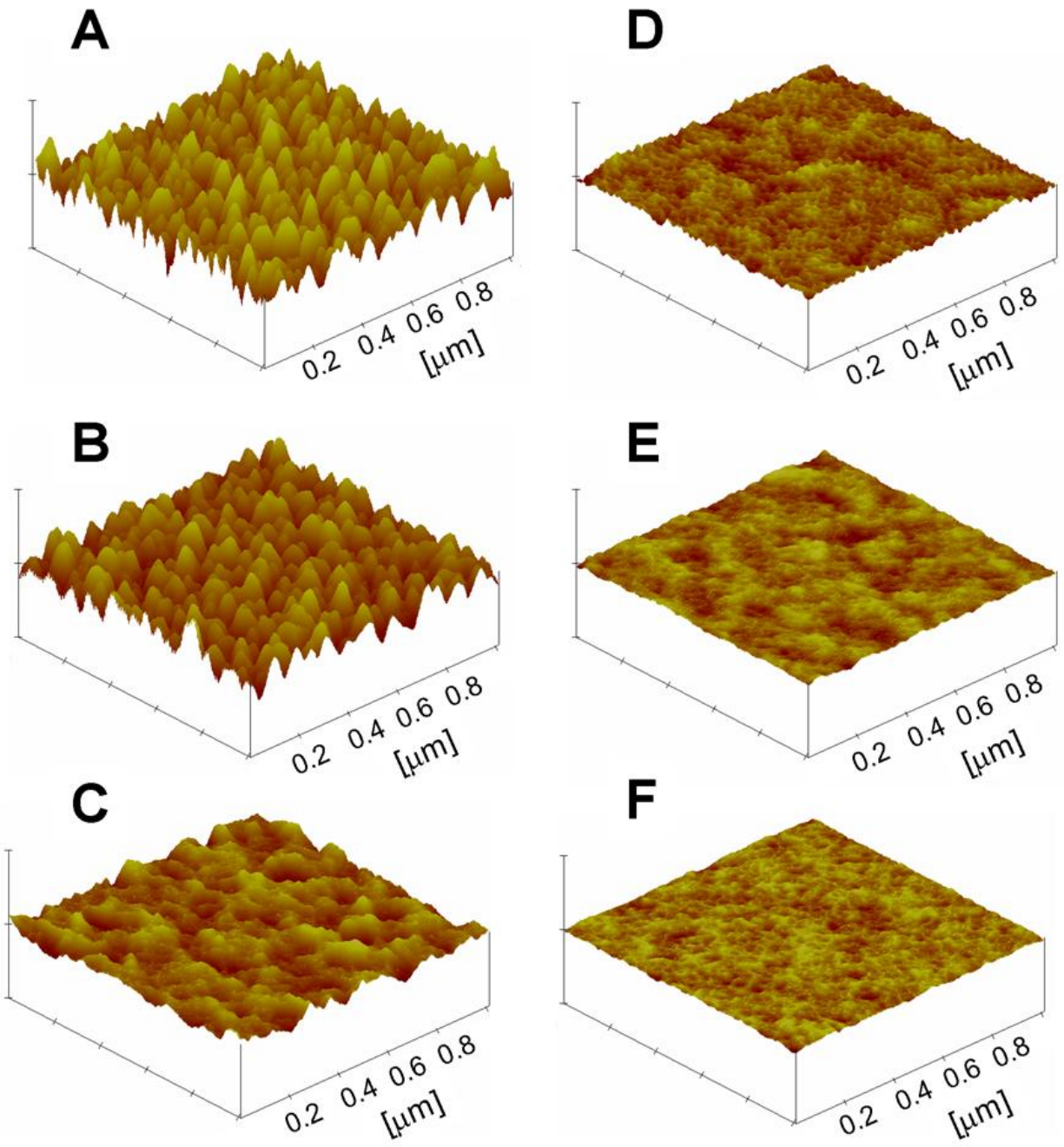

Figure 5 AFM surface topography plots for samples prepared at $f_{N2/Ar}$ = 0.1 as a function of negative bias voltage, V_S: A) self-bias, B) 40 V, C) 60 V, D) 80V, E) 100 V, and F) 150 V.

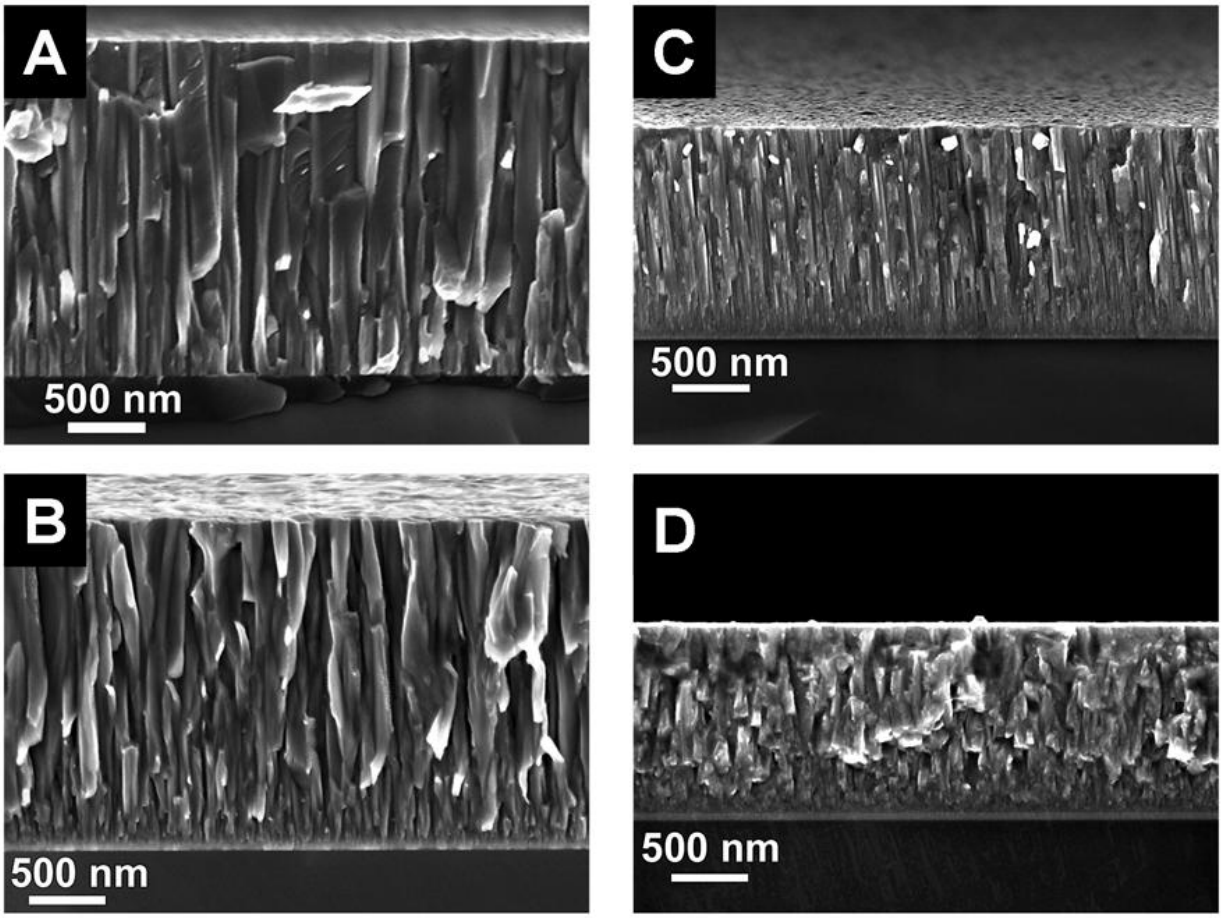

Figure 6 Fracture cross-section SEM micrographs showing the effect of substrate bias for the following cases: A) $f_{N2/Ar}$ = 0, self-bias; B) $f_{N2/Ar}$ = 0, V_s = 150 V; C) $f_{N2/Ar}$ = 0.5, self-bias, and D) $f_{N2/Ar}$ = 0.5, V_s = 150 V. The pulsing frequency was 300 Hz in all cases

discussion of the sample A film texture above) for Cr films, and from slight ⟨200⟩-oriented to ⟨111⟩-textured in the case of films with dominant CrN phase ($f_{N2/Ar} \geq 0.5$). For the latter samples, the residual compressive stress increases significantly upon application of a high bias voltage: from -4.8 GPa to -8.4 GPa in the case of $f_{N2/Ar}$ = 0.5 and from -4.6 GPa to -9.6 GPa for $f_{N2/Ar}$ = 1 (samples "I" and "I2" in Table 1). Similar to films prepared at $f_{N2/Ar}$ = 0.1, the nitrogen content in the self-biased samples is higher than in films prepared at V_s = 150 V, owing to preferential re-sputtering of nitrogen.

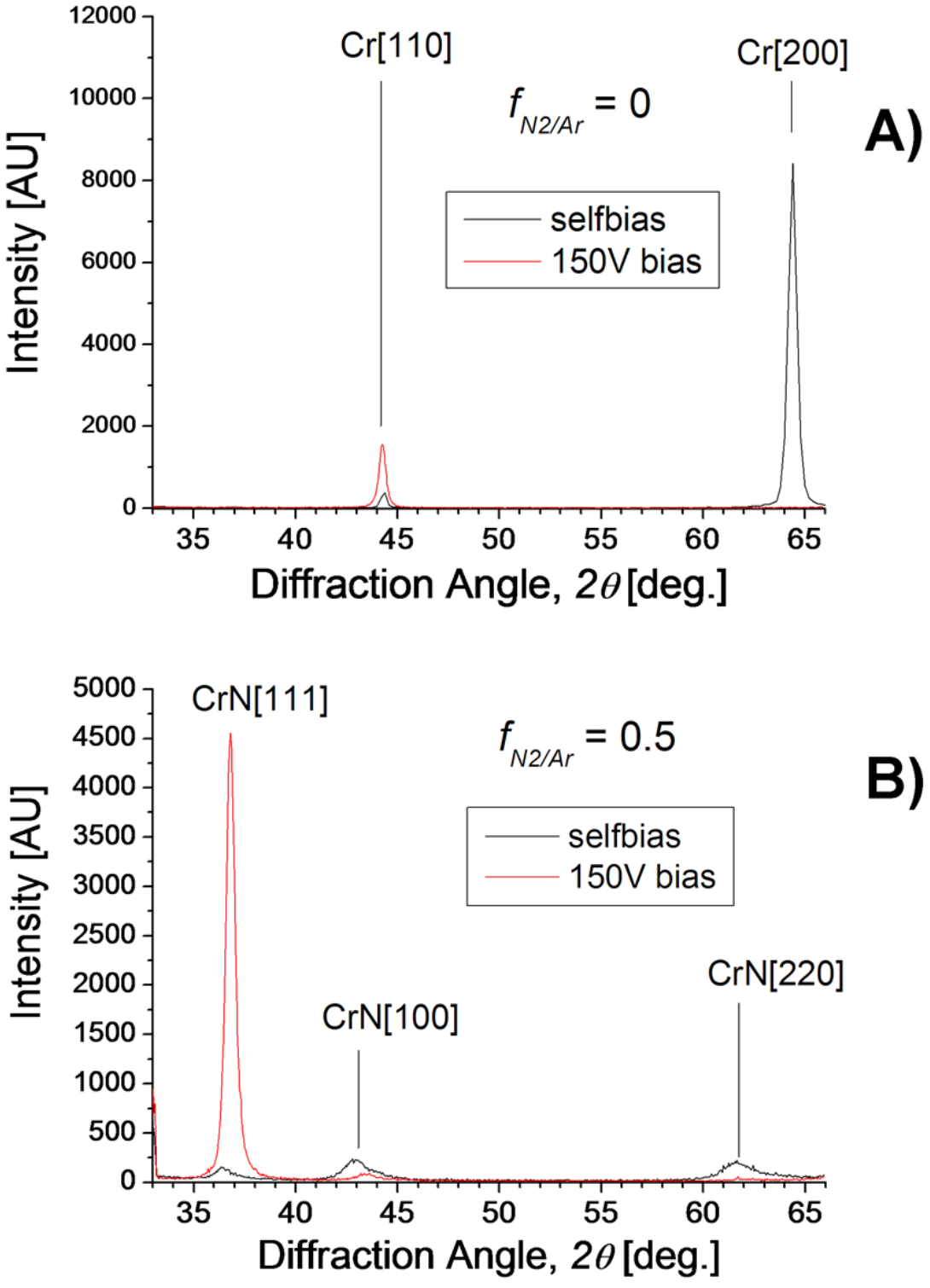

Figure 7 XRD diffractograms illustrating the effect of substrate bias at: $f_{N2/Ar}$ = 0 (A) and $f_{N2/Ar}$ = 0.5 (B).

In addition, the effect of substrate bias was also tested in combination with a lower pulsing frequency of 100 Hz (samples "C2" and "C3") and $f_{N2/Ar}$ = 0.1. In this case while going from V_s = 150 V to the self-bias condition, the nitrogen content increases from 34 at.% to 46 at.%. This is accompanied by the transition from a ⟨220⟩-textured CrN phase to the texture-free CrN. The columnar growth is to large extent suppressed at 150 V bias and develops fully at self-bias, in agreement with the phase diagram in Fig. 6. The self-bias sample ("C3") exhibits a low residual stress of -2.3 GPa, which is the lowest value of all CrN_x samples tested.

Another consequence of biasing is the preferential re-sputtering of nitrogen manifested by a decrease in both the nitrogen content as well as the total film thickness with increasing bias voltage. As evident from Fig. 1 and Table 1 this effect is present in all samples. It is perhaps less extensive in samples prepared under $f_{N2/Ar} \geq 0.5$, due to higher N_2 flows for which the incident ion flux has a different composition with more light N ions that are not so efficient in re-sputtering, and the fact that the CrN cubic lattice seem to be more resistant towards ion flux-induced degradation than the hexagonal β-Cr_2N (as evident from the strength of the XRD signal). This re-sputtering effect, often observed for CrN_x in the case of sputter-deposition sources characterized by the high flux of energetic ions [26], may be hard to avoid during HIPIMS processing due to: (i) high floating potentials present and (ii) high flux of doubly-charged Cr ions [40].

3.4 Dependence on pulse energy

The average power during HIPIMS processing is a product of the energy per pulse, E_p, and the operating frequency, f. In this section we investigate the effect of increasing the average power by varying the former quantity, while keeping the latter one constant. Here, E_p

was varied between 3.3 J and 25 J while the pulsing frequency was kept constant at 300 Hz. It is noted that increasing E_p (equivalent to increasing peak target current, as the pulse width is kept constant) affects not only the ionization level in the plasma, but also the entire ion energy spectrum gets modified (applies to both metal ions and ions of the working gas) [40]. This, together with that fact that the HIPIMS ion energy spectrum is significantly broader (in the energy space) than is the case in DC sputtering [5] makes it virtually impossible to vary the ion-to-atom ratio in the deposition flux without affecting the ion energy. These two quantities are thus inter-twined in HIPIMS.

An investigation was also performed for two different N_2-to-Ar flow ratios of $f_{N2/Ar}$ = 0.1 (cf. Fig. 8A-C)) and $f_{N2/Ar}$ = 0.5 (not shown). A moderate substrate bias of -60 V was used that did not override the effect of pulse-induced modification of the incident ion flux by too severe acceleration at the substrate. In the case of films grown at a lower N_2 flow, the nitrogen content varied between 36 at.% and 39 at.% with no clear trend *vs* E_p, thus being close to that of the self-biased sample prepared at the same pulsing frequency of 300 Hz (34 at.%, sample "C4").

As discussed above, samples with a similar N content were dominated by the β-Cr_2N phase and were prone to microstructure modifications upon increased substrate bias (cf. "C4" vs "C"). The set of cross-sectional SEM micrographs in Fig. 8 clearly shows that no such phenomena takes place upon increasing E_p from 3.3 J up to 20 J. The film microstructure is similar in all cases. In addition, XRD results (not shown) indicated a pre-dominance of the β-Cr_2N phase with a strong ⟨111⟩ texture (similar to that of sample "C4" prepared at self-bias), independently of E_p. In line with these observations, also in the case of CrN_x films grown at $f_{N2/Ar}$ = 0.5, the complete lack of changes upon increasing pulse energy was noted. All samples exhibit a columnar growth of a single phase of CrN characterized by a slight ⟨220⟩ texture in accordance

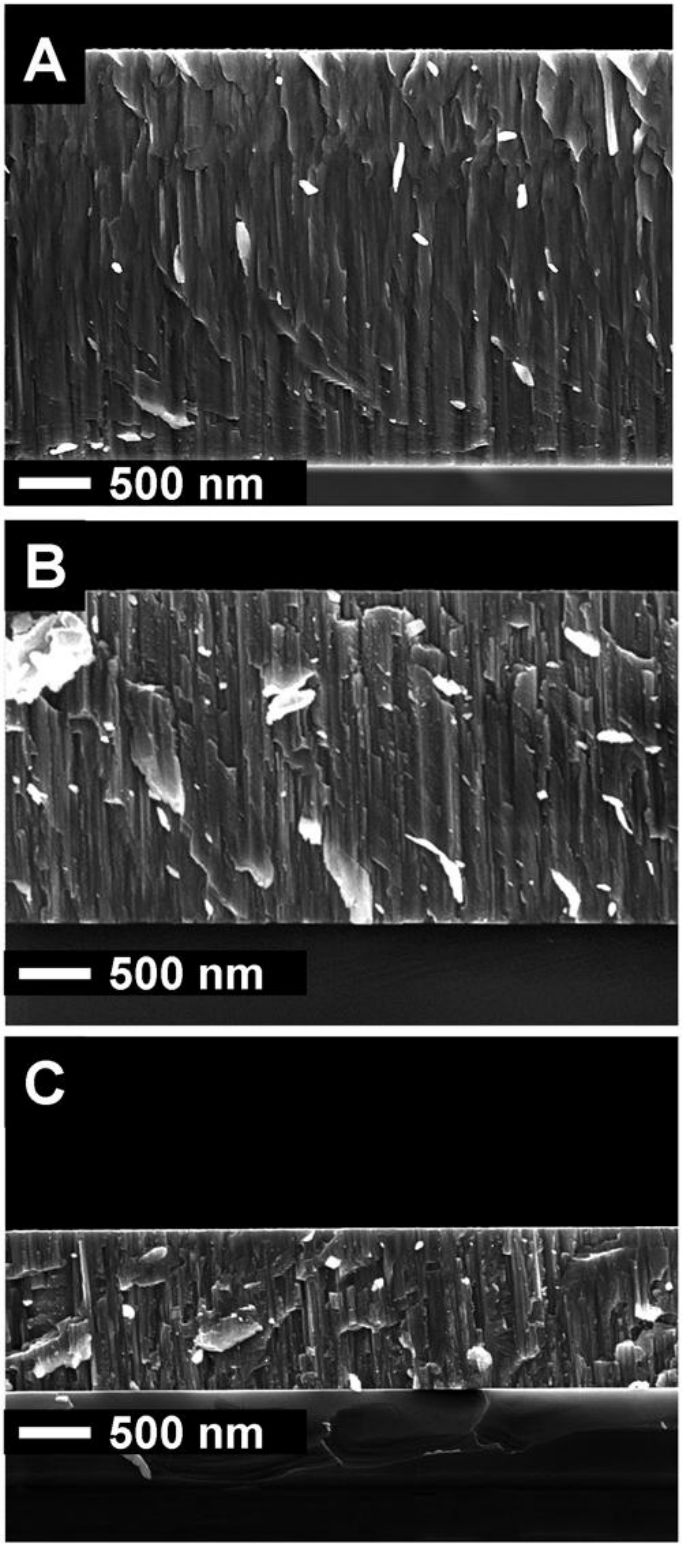

Figure 8 Set of fracture cross-section SEM micrographs for different values of pulse energy, E_p, at $f_{N2/Ar}$ = 0.1: A) E_p = 3.3 J; B) E_p = 6.7 J; and C) E_p = 20 J. Sample bias was set to 60 V.

with the sample "G2" (prepared at the self-bias). These results are in contrast to the previous report [14] where the microstructure evolution of the HIPIMS-deposited CrN_x coatings was studied as a function of the peak target current. The transition from a columnar to a nano-crystalline morphology was observed upon increasing the peak target current (what in the present terminology corresponds to an increasing E_p). It has to be emphasized, however, that the increase in the peak target current in [14] was associated with a simultaneous decrease in the pulsing frequency to keep the average current constant.

The lack of significant structural modifications upon increasing E_p is somewhat surprising especially considering the results of ion mass spectroscopy studies performed in parallel [38]. It was shown that the primary effect of increasing E_p (thus increasing the peak target current) is a strong increase in the number of doubly charged Cr ions (a factor of 8 when going from 3 J to 30 J), accompanied by a significant increase of the average ion energy (from 10.7 eV to 16.7 eV). These results were obtained while sputtering in metallic mode ($f_{N2/Ar} = 0$). Similar effects were also noted during the reactive mode of operation. Even though the increase in the total number of film-forming ions (and their average energy) is significant, the effect imposed by the application of a high bias voltage ($V_S \geq 100\,\mathrm{V}$) is more substantial. As we shall see, this is predominantly due to the presence of doubly charged Cr ions. In order to prove this point, we compare the relative ion fluxes incident upon the growing film (during the voltage pulse) in the following cases: A) E_p = 20 J and V_s = 60 V (no apparent change in the film microstructure observed) vs B) E_p = 13.3 J and V_s = 150 V (ion bombardment causes severe changes in film microstructure). We consider here only the temporal ion fluxes incident on the growing film during the active (pulse ON) phase of the discharge due to the fact that the bias voltage was synchronized with the cathode pulse and both pulses were of the same duration. The

thermalized ions that appear in the post-discharge plasma are not treated explicitly since their influence on the film growth is expected to be similar in both cases (after the pulse is over, ion fluxes do not differ that much with increasing E_p, also – the floating potential is not very high at that stage). In case A, the ion energy spectrum extends from 60 eV to 180 eV. The relative contributions to the flux are as follows: 43.0% Ar^+, 43.2% Cr^+, 12.2% Cr^{2+}, and 1.6% Ar^{2+}. The Ar^+ ions are nearly monoenergetic (on this energy scale) and form a peak slightly above 60 eV, the Cr^+ ions possess broad energy spectrum extending between 60 eV and 120 eV. Due to biasing doubly charged ions move higher up in terms of energy: the Cr^{2+} ions spread between 120 eV and 180 eV, while the Ar^{2+} ions show a low intensity peak at around 120 eV. Turning to the case B, the energy region between 150 eV and 180 eV (previously dominated by the Cr^{2+} ions) is now occupied by the Ar^+ and Cr^+ ions (due to a lower E_p the energy spectrum of Cr^+ ions becomes narrower). In addition, the high energy peak due to Cr^{2+} ions appears between 300 eV and 330 eV. The relative contributions to the flux in case B are as follows: 60.2% Ar^+, 30.8% Cr^+, 7.0% Cr^{2+}, and 2.0% Ar^{2+}. A comparison between cases A and B reveals two major differences: (i) the flux of Cr^{2+} ions in case A (E_p = 20 J, V_s = -60 V) overlaps in terms of energy with a combined flux of Ar^+ and Cr^+ ions present in case B (E_p = 13.3 J, V_s = -150 V), and constitutes roughly half the intensity of the combined flux; (ii) the significant flux of Cr^{2+} ions (with a minor contribution from the Ar^{2+} ions) with energies between 300 eV and 330 eV is unique to case B. It is therefore suggested that the column-free microstructure observed under high bias voltage is primarily due to the highly energetic flux of Cr^{2+} ions, that does not have any equivalent in case A. On the other hand, the effect caused by a combined flux of Cr^+ and Ar^+ ions (that in case B have energies between 150 eV and 180 eV) is also present in case A due to the flux of Cr^{2+} ions that posses similar energy, therefore it can not account for the observed difference in film microstructure. Thus, even though the pulse energy has no *direct* effect on a microstructure of the growing film

(as analyzed by XRD and SEM) it may induce structural changes *indirectly*, by means of altering the flux of doubly charged Cr ions that, if a sufficiently high bias is applied, leads to a substantial modification of the film growth mode.

The direct and very pronounced effect of the increasing pulse energy is a loss of power-normalized deposition rate, as indicated in Fig. 9. Independent of gas composition ($f_{N2/Ar}$ = 0.1 or $f_{N2/Ar}$ = 0.5) a similar effect is observed. After the initial (nearly linear) increase up to E_p = 12 J, the deposition rate tends to saturate at higher values of the pulse energy (cf. black curves). In consequence, the efficiency of the sputtering process goes down with increasing E_p, as indicated by a continuous drop in the power-normalized deposition rate (cf. red curves). Upon increasing the pulse energy from 3.3 J to 25 J the growth rate per kW of a supplied power goes down by a factor of 3. It should be added that all deposition rates presented in Fig. 9 are derived from SEM cross-sections of samples where no obvious effect of E_p on the microstructure of the growing films was observed (as discussed above). Therefore, any variations in film thickness with changing E_p are believed to reflect the actual variations in the depositing flux while potential changes in film density can be neglected.

The trends outlined in Fig. 9 touch upon an early noted limitation of HIPIMS – the low deposition rate relative to the conventional DC sputtering rate at the corresponding power level [10,41-43]. In the present work the HIPIMS deposition rate constitutes 48.7% of a DC rate at 3.3 J per pulse and drops further down to 19.9% in the case of deposition with 25 J pulses. This trend is ascribed to the fact that with increasing E_p (thus increasing target current) the degree of metal ionization increases, leading to the situation where a larger fraction of the sputtered material gets captured by the cathode potential (causing re-sputtering). Since ionization of the target material is significantly higher in HIPIMS than in the conventional DC sputtering, the effect is by far more pronounced in the former case. In order to verify the trends in deposition

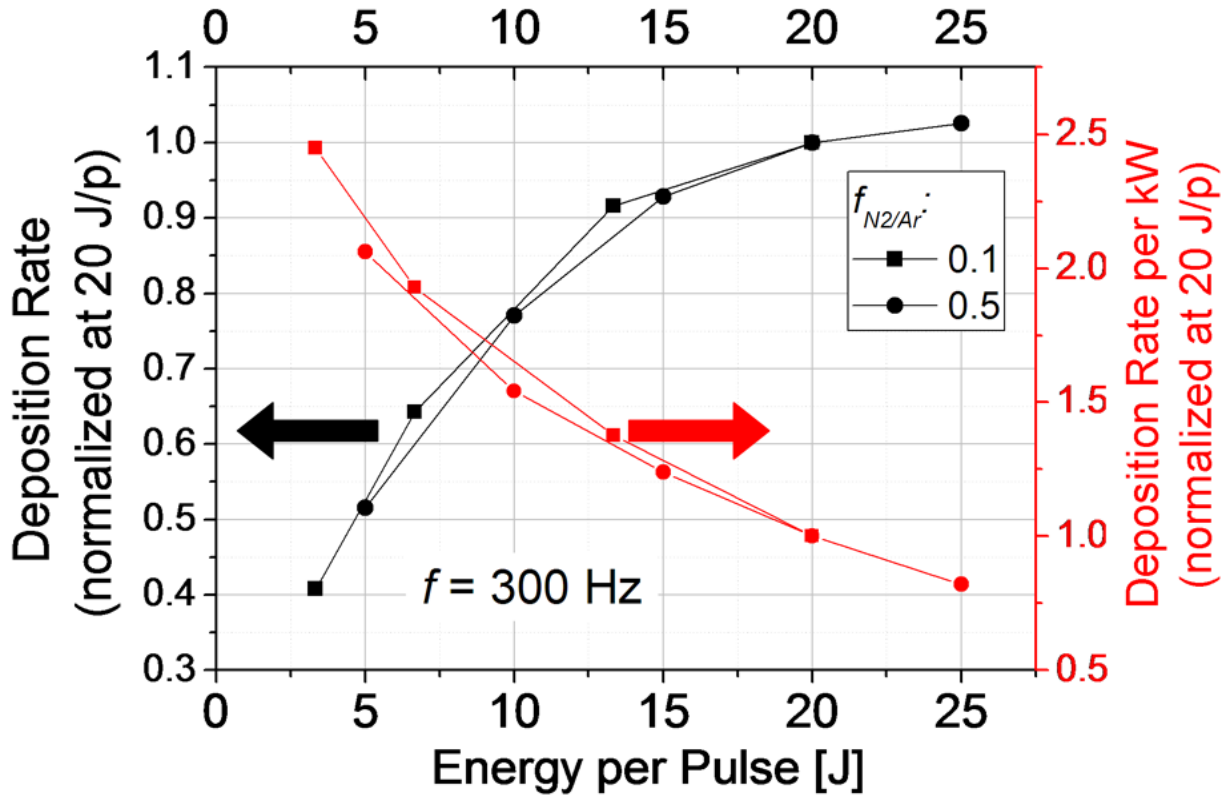

Figure 9 Deposition rate as a function of pulse energy for $f_{N2/Ar}$ = 0.1 (squares) and $f_{N2/Ar}$ = 0.5 (circles). On the left axis (black data points) the actual rate was normalized to the value measured at 20 J. On the right axis (red data points) deposition rate per kW (normalized at 20 J) is plotted.

rate with increasing degree of metal ionization optical emission spectroscopy (OES) was used to characterize the HIPIMS plasma at different values of E_p. The intensity of the emission lines from Cr^+ ions (*Cr II* at 336.9 nm) and Cr neutrals (*Cr I* at 399.2 nm) was measured as a function of E_p for various N_2-to-Ar flow ratios, $f_{N2/Ar}$. The emission lines with similar excitation energy were chosen (5.67 eV for neutrals and 6.16 eV for ions, respectively) in order to minimize the emission intensity changes caused by a potential variation of the electron distribution function with increasing E_p. The OES data were then used to plot in Fig. 10 the HIPIMS deposition rate normalized to the DC rate as a function of the relative intensity of the *Cr II* emission line (*Cr II/(Cr II+Cr I)*). The latter quantity represents *relative* changes of the ion content in the plasma

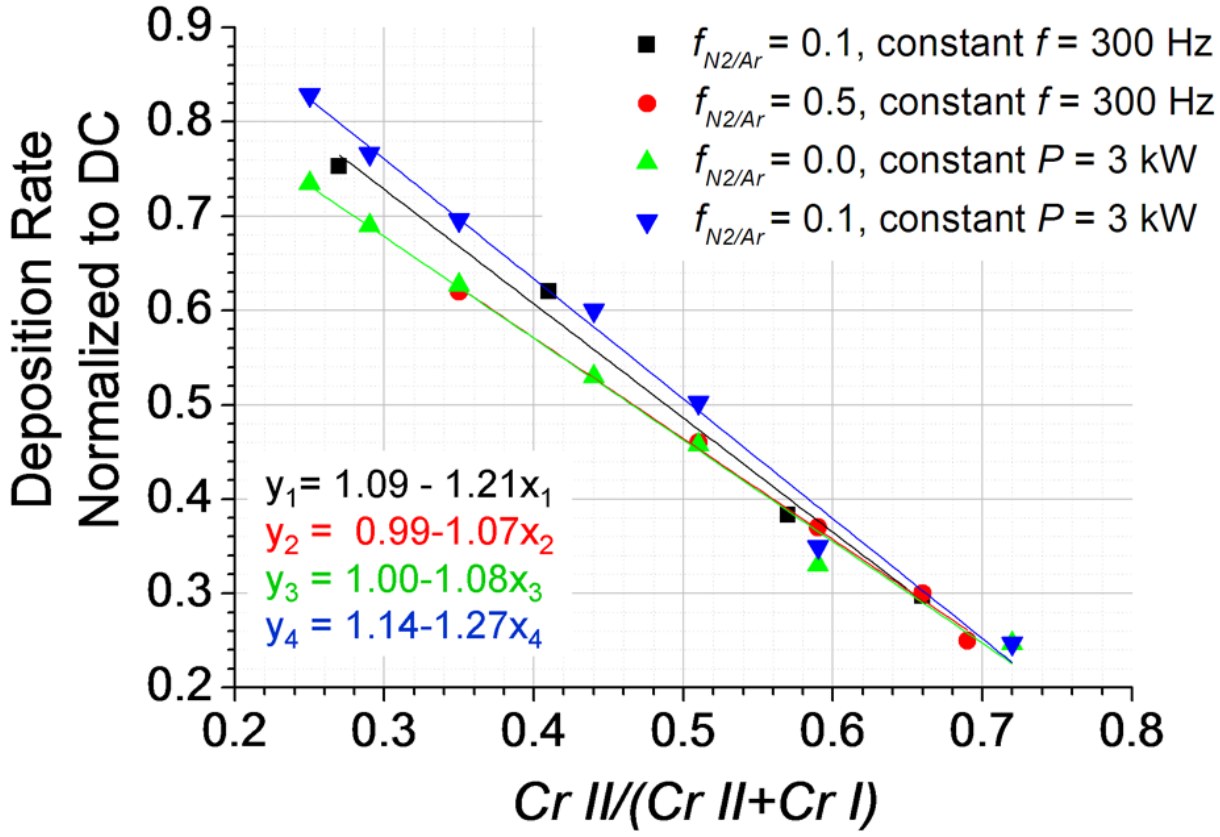

Figure 10 Deposition rate normalized to the DC rate (at the same average power), plotted as a function of relative intensity of the *Cr II* emission line assigned to Cr^+ ions. Data points are shown for operation at the constant frequency of 300 Hz (black and red), as well as, at the constant average power (green and blue). The experiment was performed for different values of $f_{N2/Ar}$ as indicated in the legend. Results of linear fitting are given in the left-bottom corner.

with varying process parameters (E_p, $f_{N2/Ar}$, etc.), as the measurement of ionization degree in *absolute* terms is not trivial. Data were acquired versus increasing E_p at the constant frequency of 300 Hz (black and red plots), as well as, at the constant average power of 3 kW (green and blue plots). In all cases a linear drop of a normalized deposition rate with increasing relative strength of *Cr II* emission line is observed. A linear fitting results in intercept values between 0.99 and 1.14, while the slope is between 1.07 and 1.27. Interestingly, the linear relationship of the form $\alpha = 1 - \beta$ between a normalized deposition rate, α, and the ionized fraction of a metal flux, β, has

been derived as a particular case of the target pathways model [12]. This expression was namely found for those combinations of the target material and a working gas where: a) the self-sputtering rate is approximately equal to the sputtering rate and b) a majority of target ions gets captured by the target. While the former condition is readily satisfied in the case of Cr target sputtering in Ar [12], the applicability of the latter one is difficult to assess. The ion capturing efficiency approaching unity would imply that essentially no ions are reaching the substrate, which is in contradiction to the ion mass spectroscopy studies that reveal high ion count rates at relatively large distance from the target surface (21 cm). This paradox can possibly be resolved if the majority of the ions detected at the substrate position are created further away from the target (as was, in fact, proposed in the extension of the path-ways model [13]), giving only a minor contribution to the OES signal (as they reside in a lower plasma density region). The intensity of the *Cr II* spectral line would then reflect relative changes in the ion content within the cathode fall region only, resulting in a good correlation to the observed drop in deposition rate.

3.5 Dependence on the pulsing frequency

The effect of increasing the average HIPIMS power by increasing the pulsing frequency, while keeping the energy per pulse constant is illustrated in Fig. 11 with fracture cross-section SEM micrographs . Two series of samples were examined: (i) $f_{N2/Ar}$ = 0.1 deposited at the floating potential (Fig. 11A-C) and (ii) $f_{N2/Ar}$ = 0.2 grown at V_s = 150 V (Fig. 11D-F). In both cases, increasing frequency leads to a finer grain structure and suppression of the columnar growth. The sample sputtered at $f_{N2/Ar}$ = 0.1 and f = 100 Hz contains 46 at.% nitrogen and is composed of CrN grains with no apparent texture. As the frequency is increased to 300 Hz, the nitrogen content drops to 34 at.% and the sample is dominated by the β-Cr_2N phase with $\langle 111 \rangle$

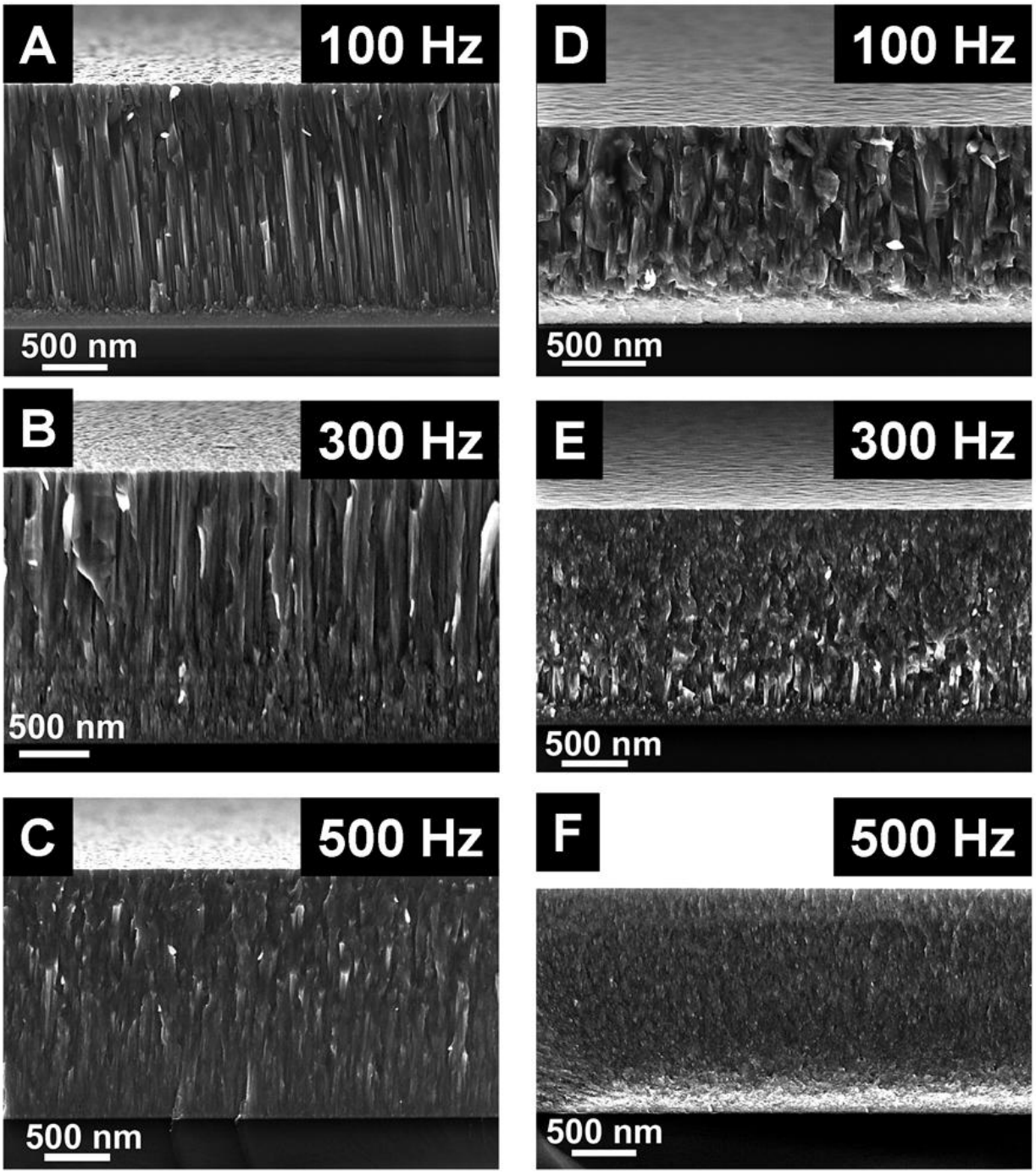

Figure 11 Effect of pulsing frequency on the microstructure of growing film illustrated with fracture cross-section SEM micrographs: A-C) $f_{N2/Ar}$ = 0.1, self-bias; D-F) $f_{N2/Ar}$ = 0.2, V_s = 150 V.

texture. Increasing frequency even further to 500 Hz results in a film with a less columnar character, containing 31 at.% N and composed of ⟨111⟩-textured β-Cr_2N grains. A similar trend is

also observed at $f_{N2/Ar}$ = 0.2 and V_s = 150 V for which the nitrogen content decreases from 46 at.% to 35 at.% when increasing the pulsing frequency from 100 Hz to 500 Hz. At the same time the growth mode evolves from columnar (cf. Fig. 11D) to structure-less (Fig. 11F)), while the crystalline structure changes from being CrN-dominated to β-Cr_2N-dominated.

Even though the drop in the nitrogen content with increasing pulsing frequency could be expected, it can be concluded from the above observation that the dependence of film structure on frequency (at the constant E_p) can not be simply reduced to being the equivalent of a varying nitrogen flow. Films prepared at high frequency (500 Hz) tend to have smaller grains and less pronounced columnar structure than films containing similar amounts of nitrogen, but grown at lower frequency. Useful examples here are the column-free sample "E2" (cf. Table 1 and Fig. 11F) grown at f = 500 Hz, $f_{N2/Ar}$ = 0.2 and V_s = 150 V (35 at.% N) and the sample denoted "C2" (f = 100 Hz, $f_{N2/Ar}$ = 0.1 and V_s = 150 V). Despite a similar nitrogen content (34 at.%) the latter sample retains a quite columnar character. The effect can be explained with the help of ion mass spectroscopy measurements revealing that sputtering at higher frequency results in a higher average energy of the film-forming ions arriving at the substrate [38]. This is due to the fact that the relative contribution of the high-energy tail (ions leaving the target with energies higher than 20 eV) to the time-averaged ion distribution function increases with increasing frequency [38]. In other words, at higher frequency the growing film is more often exposed to the high energy ions. When depositing at floating potential, the effect may be to some extent counteracted by the fact that the maximum self-bias voltage tends to decrease with increasing pulsing frequency, as discussed above. Perhaps for this reason the completely column-free films (of the type obtained at 150 V bias, cf. Fig. 11C and Fig. 2B-C) could not be prepared at a lower bias voltage even if a high pulsing frequency was used. It can be concluded by comparing the microstructures shown in

Fig. 11C and 11F that a high bias voltage is a necessary condition to produce completely column-free films. Both films are dominated by the β-Cr_2N phase and the nitrogen content is similar, still it is only the sample prepared at V_s = 150V bias that has a column-less structure.

While discussing the effect of the pulse energy on the power-normalized deposition rate it was shown that a severe drop is observed with increasing E_p, what was attributed to the fact that the increasing fraction of the energy delivered in each pulse is lost to the back-attracted ions. In order to increase the understanding the dependence of a deposition rate on the pulsing frequency at the *constant* average power of 3 kW was studied, and the results for the case of metallic deposition ($f_{N2/Ar}$ = 0) are shown in Fig. 12. As expected, the deposition rate increases with increasing frequency: from ~25 % of the DC rate at 100 Hz up to ~74% of the DC rate at 1 kHz. Note that at the same time E_p decreases from 30 J to 3 J. The observed nearly three-fold gain in the deposition rate takes place at the expense of the relative ion content in the plasma, which goes down by the corresponding factor (cf. Fig. 10).

The dependence of the deposition rate on the pulsing frequency can be predicted using the relationship between the deposition rate and E_p at a fixed frequency of 300 Hz (data presented in Fig. 9). As evident from Fig. 9 the dependence of the deposition rate on E_p is described by the function that is independent of $f_{N2/Ar}$, which indicates a more general character of this relationship. This is probably the reason for the good data fit obtained in Fig. 12 for $f_{N2/Ar}$ = 0. The rate per pulse, γ_p, varies with E_p as:

$$\gamma_p \propto \left[1 - \exp\left(-\frac{E_p}{E_0}\right)\right], \qquad (1)$$

where E_0 = 7.24 J and the proportionality constant is $f_{N2/Ar}$-dependent. Using the fact that the average power is a product of the pulsing frequency and the energy per pulse, $\langle P \rangle = fE_p$, and

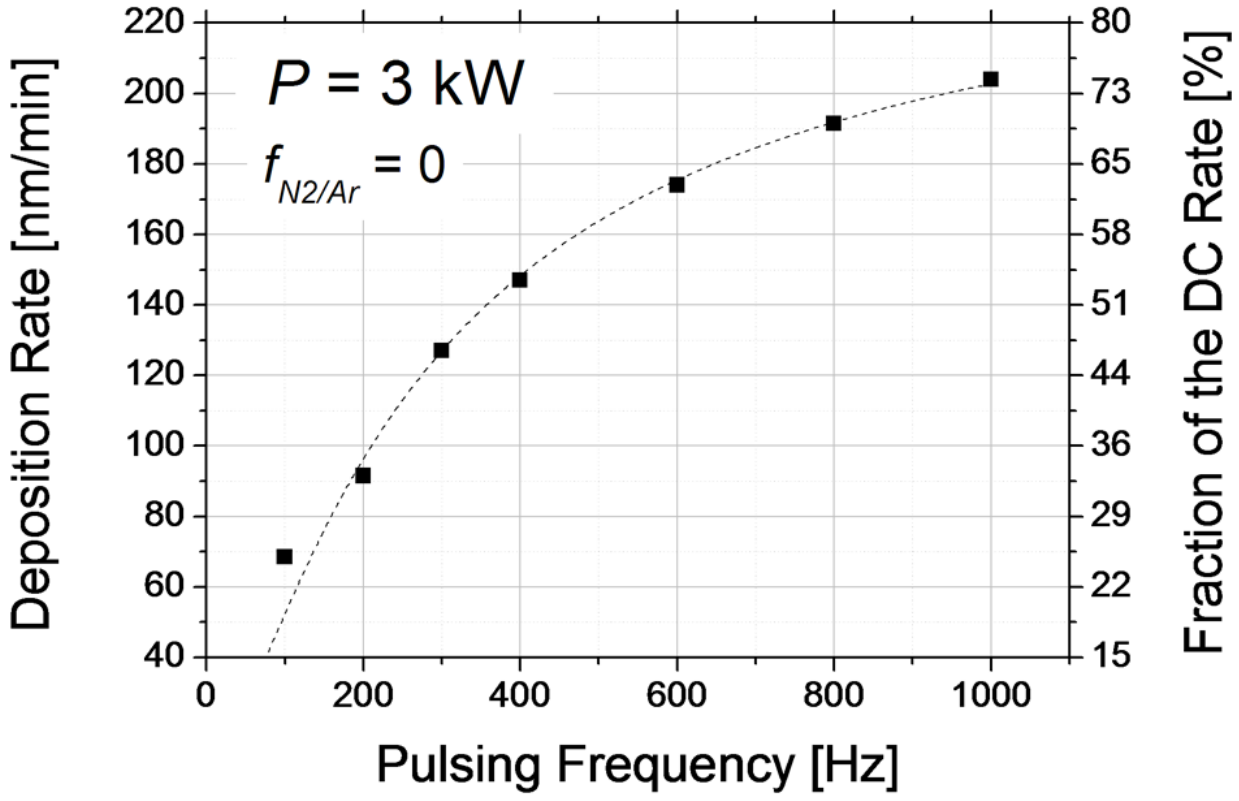

Figure 12 Deposition rate as a function of pulsing frequency at the constant average power mode of HIPIMS operation. On the right axis the HIPIMS rate is expressed as a fraction of DC rate at the same average power of 3 kW. The dashed line represents the empirical prediction (cf. Eq. 2 in the text) based on the dependence of deposition rate on E_p at the constant frequency of 300 Hz.

taking into account that the deposition rate per time interval Δt is $\gamma = Nf\gamma_p$ (where Nf represents the number of pulses in the time interval Δt), the dependency of the deposition rate (in nm/Δt) on the pulsing frequency in the constant power mode can be rewritten as

$$\gamma = ANf\left[1-\exp\left(-\frac{\langle P\rangle}{fE_0}\right)\right], \qquad (2)$$

where A is a proportionality constant. The corresponding data fit presented in Fig. 12 is $N = 60$, $A = 9.44\times10^{-3}$ nm and $\langle P \rangle = 3000$ W. The applicability of this equation can be verified by exploiting the limit of the high frequency ($f \to \infty$) that physically represents the case of a DC sputtering. By using the Taylor expansion of the exponential function in Eq. (2) it can be shown that for large f, Eq. (2) reduces to

$$\gamma_{f\to\infty} = \frac{AN\langle P \rangle}{E_0}. \qquad (3)$$

In the present case Eq. (3) yields 234.7 nm/min, which underestimates the experimental value by only 8% as measured in the reference experiment.

4. CONCLUSIONS

The stoichiometry of CrN_x films deposited by reactive HIPIMS is entirely determined by the composition of the material flux incident upon the substrate during the active phase of the discharge, and no N_2 uptake takes place at the substrate between the high-power pulses.

For $0 < f_{N2/Ar} < 0.15$ and $V_s = 150$ V, the columnar growth is suppressed and the films consist of a nano-sized grains. This results in an extremely flat surface topography. The column-free films are dominated by Cr(N) or β-Cr_2N phases and form for nitrogen contents less than 33 at.%. The loss of columnar structure in the case of films with low nitrogen content is a unique feature of HIPIMS. The microstructure of CrN_x films prepared within this regime shows a high sensitivity to the bias voltage. As the amplitude of the V_S decreases, the film morphology

evolves from the column-free ($100\,\mathrm{V} \leq V_S \leq 150\,\mathrm{V}$) into a dense columnar structure observed at V_s = 40 V and for the self-biased films. This is accompanied by a corresponding increase in the average surface roughness from 0.25 nm to 2.4 nm. Films prepared at $f_{N2/Ar}$ = 0 or $f_{N2/Ar}$ = 0.5 (and higher) show columnar growth, independently of the applied bias voltage and only the film texture is affected. The residual compressive stress increases significantly upon the application of a high bias voltage: from -4.8 GPa to -8.4 GPa in the case of $f_{N2/Ar}$ = 0.5 and from -4.6 GPa to -9.6 GPa for $f_{N2/Ar}$ = 1. A finer grain structure may also be obtained in CrN_x samples prepared at higher frequency what is attributed to the increased time-averaged mean energy of film-forming ions arriving at the substrate. The high bias voltage is, however, necessary to produce column-free films. The latter effect is ascribed to the high flux of doubly charged Cr ions.

The power-normalized deposition rate decreases with increasing E_p, independent of $f_{N2/Ar}$, what is found to be closely related to the increased ion content in the plasma. The empirical relationship between the HIPIMS deposition rate and relative ion content in the plasma closely follows the prediction of the target pathways model for the special case where (i) the self-sputtering rate is approximately equal to the sputtering rate and ii) a majority of target ions gets captured by the target. When operating in the *constant* average power mode and $f_{N2/Ar}$ = 0 the deposition rate was shown to increase from 25% of the DC rate at 100 Hz (E_p = 30 J) up to ~74% of the DC rate at 1 kHz (E_p = 3 J). The observed, nearly three-fold, gain in deposition rate takes place at the exact expense of the relative ion content in the plasma.

ACKNOWLEDGEMENTS

We thank the staff at the Tandem Laboratory, Uppsala University, for technical assistance with the ToF-ERDA analysis. The financial support from the European Research Council (ERC) through an Advanced Grant is also acknowledged.

REFERENCES

[1] V. Kouznetsov, K. Macak, J. M. Schneider, U. Helmersson and I. Petrov, *Surface and Coatings Technology* **122** (1999), p. 290.

[2] J. Bohlmark, J. T. Gudmundsson, J. Alami, M. Lattemann and U. Helmersson, *IEEE Transactions on Plasma Science* **33** (2005), p. 346.

[3] A. P. Ehiasarian, R. New, W.-D. Munz, L. Hultman, U. Helmersson and V. Kouznetsov, *Vacuum* **65** (2002), p. 147.

[4] J. T. Gudmundsson, J. Alami and U. Helmersson, *Surface and Coatings Technology* **161** (2002), p. 249.

[5] J. Bohlmark, J. Alami, C. Christou, A. P. Ehiasarian and U. Helmersson, *Journal of Vacuum Science & Technology A (Vacuum, Surfaces, and Films)* **23** (2004), p. 18.

[6] J. Bohlmark, M. Ostbye, M. Lattemann, H. Ljungcrantz, T. Rosell and U. Helmersson, *Thin Solid Films* **515** (2006), p. 1928.

[7] I. Petrov, P. B. Barna, L. Hultman and J. E. Green, *Journal of Vacuum Science & Technology A (Vacuum, Surfaces, and Films)* **21** (2003), p. S117.

[8] J. Alami, K. Sarakinos, G. Mark and M. Wuttig, *Applied Physics Letters* **89** (2006), p. 154104.

[9] U. Helmersson, M. Lattemann, J. Bohlmark, A. P. Ehiasarian and J. T. Gudmundsson, *Thin Solid Films* **513** (2006), p. 1

[10] K. Sarakinos, J. Alami, S. Konstantinidis, *Surface and Coatings Technology* **204** (2010) 1661–1684

[11] J. A. Hopwood, Editor, Ionized Physical Vapor Deposition, Academic Press, San Diego, San Diego (2000).

[12] D. J. Christie, *Journal of Vacuum Science and Technology A* **23** (2005), p. 330.

[13] J. Vlcek, P. Kudlacek, K. Burcalova and J. Musil, *Jornal of Vacuum Science and Technology A* **25** (2007), p. 42.

[14] J. Alami, K. Sarakinos, F. Uslu and M. Wuttig, *Journal of Physics D: Applied Physics* **42** (2009), p. 015304.

[15] K. Bobzin, N. Bagcivan, P. Immich, S. Bolz, R. Cremer and T. Leyendecker, *Thin Solid Films* **517** (2008), p. 1251.

[16] A. P. Ehiasarian, W.-D. Munz, L. Hultman, U. Helmersson and I. Petrov, *Surface and Coatings Technology* **163-164** (2003), p. 267.

[17] P. E. Hovsepian, C. Reinhard and A. P. Ehiasarian, *Surface & Coatings Technology* **201** (2006), p. 4105.

[18] S. Konstantinidis, J. P. Dauchot and M. Hecq, *Thin Solid Films* **515** (2006), p. 1182.

[19] S. Konstantinidis, A. Hemberg, J. P. Dauchot and M. Hecq, *Jornal of Vacuum Science and Technology B* **25** (2007), p. L19.

[20] J. Paulitsch, P. H. Mayrhofer, W.-D. Münz and M. Schenkel, *Thin Solid Films* **517** (2008), p. 1239.

[21] G. Sáfrán, C. Reinhard, A. P. Ehiasarian, P. B. Barna, L. Székely, O. Geszti and P. E. Hovsepian, *Journal of Vacuum Science and Technology A* **27** (2009), p. 174

[22] V. Sittinger, F. Ruske, C. Gerloff, W. Werner, B. Szyszka and D. J. Christie, Deposition of high conductivity ITO films by High Power Pulsed Magnetron Sputtering (HPPMS), *49th Annual Technical Conference* (2006).

[23] E. Wallin, T. I. Selinder, M. Elfwing and U. Helmersson, *Europhysics Letters* **82** (2008), p. 36002.

[24] R. Mientus and K. Ellmer, *Surface and Coatings Technology* **116-119** (1999), p. 1093.

[25] P. H. Mayrhofer, G. Tischler and C. Mitterer, *Surface and Coatings Technology* **142-144** (2001), p. 78.

[26] M. Odén, C. Ericsson, G. Hakansson and H. Ljungcrantz, *Surface and Coatings Technology* **114** (1999), p. 39.

[27] M. Odén, J. Almer and G. Hakansson, *Surface and Coatings Technology* **120-121** (1999), p. 272.

[28] T. Hurkmans, D. B. Lewis, J. S. Brooks and W.-D. Munz, *Surface and Coatings Technology* **86-87** (1996), p. 192.

[29] A. Ehrlich, M. Kuhn, F. Richter and W. Hoyer, *Surface & Coatings Technology* **76-77** (1995), p. 280.

[30] C. Rebholz, H. Ziegele, A. Leyland and A. Matthews, *Surface and Coatings Technology* **115** (1999), p. 222.

[31] E. Forniés, R. E. Galindo, O. Sánchez and J. M. Albella, *Surface & Coatings Technology* **200** (2006), p. 6047.

[32] *http://www.cemecon.de/information/news/hppms__high_plasma_ionisation/index_eng.html*.

[33] M. S. Janson, *Internal Report, Uppsala University* (2004).

[34] M. Birkholz, Thin Film Analysis by X-ray Scattering, WILEY-VCH, Weinheim (2006).

[35] R. L. Kurucz and B. Bell, 1995 Atomic Line Data (R.L. Kurucz and B. Bell) Kurucz CD-ROM No. 23. Cambridge, Mass.: Smithsonian Astrophysical Observatory., In: M. S. A. O. Cambridge, Editor.

[36] C. Christou and Z. H. Barber, *Journal of Vacuum Science and Technology A* **18** (2000), p. 6.

[37] W. Ensinger and M. Kiuchi, *Surface & Coatings Technology* **94-95** (1997), p. 433.

[38] G. Greczynski and L. Hultman, *Vacuum* **84** (2010) 1159-1170

[39] A. E. McHale, Editor, Phase Equilibrium Diagrams - Borides, Carbides and Nitrides, The American Ceramic Society, Westerville, OH (1994).

[40] A. Hecimovic and A. P. Ehiasarian, *Journal of Physics D: Applied Physics* **42** (2009), p. 135209.

[41] J. A. Davis, W. D. Sproul, D. J. Christie and M. Geisler, High Power Pulse Reactive Sputtering of TiO2, *Society of Vacuum Coaters 47th Annual Technical Conference Proceedings* Dallas, TX USA (2004).

[42] D. A. Glocker, M. M. Romach, D. J. Christie and W. D. Sproul, High Power Pulsed Reactive Sputtering of Zirconium Oxide and Tantalum Oxide, *Society of Vacuum Coaters 47th Annual Technical Conference Proceedings*, Dallas, TX USA (2004).

[43] W. D. Sproul, D. J. Christie and D. C. Carter, The Reactive Sputter Deposition of Aluminum Oxide Coatings Using High Power Pulsed Magnetron Sputtering (HPPMS), *Society of Vacuum Coaters 47th Annual Technical Conference Proceedings*, Dallas, TX USA (2004).